LA-9717-MS

Los Alamos National Laboratory is operated by the University of California for the United States Department of Energy under contract W-7405-ENG-36.

ZT-40M Current Risetime Study

Los Alamos
Los Alamos National Laboratory
Los Alamos, New Mexico 87545

Printed in the United States of America
Available from
National Technical Information Service
US Department of Commerce
5285 Port Royal Road
Springfield, VA 22161

Microfiche (A01)

Page Range	NTIS Price Code	Page Range	NTIS Price Code	Page Range	NTIS Price Code	Page Range	NTIS Price Code
001-025	A02	151-175	A08	301-325	A14	451-475	A20
026-050	A03	176-200	A09	326-350	A15	476-500	A21
051-075	A04	201-225	A10	351-375	A16	501-525	A22
076-100	A05	226-250	A11	376-400	A17	526-550	A23
101-125	A06	251-275	A12	401-425	A18	551-575	A24
126-150	A07	276-300	A13	426-450	A19	576-600	A25
						601-up*	A99

*Contact NTIS for a price quote.

LA-9717-MS

UC-20f
Issued: October 1983

LA--9717-MS

DE84 003563

ZT-40M Current Risetime Study

J. A. Phillips
L. C. Burkhardt
A. Haberstich
R. B. Howell
J. C. Ingraham
E. M. Little
K. S. Thomas
R. G. Watt
P. G. Weber

Los Alamos National Laboratory
Los Alamos, New Mexico 87545

ZT-40M CURRENT RISETIME STUDY

by

J. A. Phillips, L. C. Burkhardt, A. Haberstich, R. B. Howell,
J. C. Ingraham, E. M. Little, K. S. Thomas, R. G. Watt, and P. G. Weber

ABSTRACT

A study of discharge risetimes was undertaken in the reversed-field pinch (RFP) experiment, ZT-40M, to obtain guidelines for future larger and slower experiments. The electrical circuits allowed nominal risetimes of 0.25 to 1.5 ms and peak toroidal currents were $\lesssim$ 180 kA. For the longer risetimes optimized operation occurs at higher fill pressures which leads to larger radiation losses, a larger poloidal flux consumption, and a larger fraction of the energy input being lost by the time of peak toroidal current.

The maximum axial electron temperature increases with toroidal current and with peak currents of ~ 180 kA reaches ~ 300 eV with all risetimes. The early, very rapid, density pumpout ends near the time of toroidal field reversal, and there is a critical low-density limit, $\sim 2 \times 10^{19}$ m^{-3}, at the time of field reversal below which RFP formation is unreliable. The rate of density pumpout is independent of risetime, so that with still longer risetimes in the larger experiments it is likely that gas puffing during RFP formation will be necessary. Gas puffing will also allow reducing the initial fill pressure thereby reducing the radiation losses during early start-up.

The amount of the major impurity (oxygen) does not change appreciably with different risetimes. Neutral nickel and chromium line radiation increase with risetime during start-up, suggesting more wall contact at longer risetimes; but after start-up, the radiated power levels are not significantly different for the various risetimes.

The study on ZT-40M with risetimes $\lesssim$ 1.5 ms indicates that for the larger RFP experiment, ZT-H, the volt·second consumption is well within design limits, gas puffing during start-up may be necessary, influx of impurities from the discharge walls may be manageable, and burnthrough of impurities can be achieved.

I. INTRODUCTION

In present reversed-field pinch (RFP) experiments at Los Alamos on ZT-40M successful RFP discharges are routinely established with toroidal current durations $\gtrsim$ 20 ms.[1] Magnetic field distributions close to those predicted[2] theoretically are formed[1] which confine plasma at high beta, 10-15%; low-Z impurities are burned through early in the discharge cycle and electron temperatures $\gtrsim$ 300 eV are reported[1] regularly. These results encourage, with plasma parameters approaching closely those in thermonuclear fusion reactors, the designers of larger and more powerful experiments.

The future RFP experiments require a considerably increased capability in the electrical drivers over present experiments. The higher energy requirements are not a major concern since large quantities of energy are available in conventional rotating machinery. The time interval, however, during which the energy is transferred to the experiment in the RFP formation phase is important. A simple extrapolation of present experiments leads to prohibitive electrical powers. The power can be made smaller, of course, by lengthening the RFP formation time, which initially is 0.25 ms. However, if the risetime is slowed down it is uncertain whether an RFP can successfully be established. With longer risetimes burnthrough of impurities might become difficult or impossible. The plasma resistance may remain high with rapid field diffusion and the loss of RFP field profiles. Loss of particle density during RFP formation, seen in present experiments,[1] may so reduce the plasma density that current-driven instabilities become important in that they lead to early discharge termination.

This study of discharge risetimes was undertaken, therefore, to obtain guidelines for the larger and slower experiments now being proposed. The study focuses on the following points as the risetime is increased:

- The operating "window" in initial gas fill-pressures, toroidal bias magnetic fields, and rates of toroidal field reversal at the wall, in which well-behaved RFP's can be formed.
- The consumption of poloidal flux (V•s input) from the toroidal current circuit during RFP formation.
- The energy input and energy loss required to establish the RFP.

- Burnthrough of impurities, present in the filling gas or released from the wall during start-up, and the energy lost by radiation.
- The plasma temperatures achieved with the longer risetimes.
- Plasma pumpout during the formation phase and the density limits for RFP formation.

II. ZT-40M OPERATION

The toroidal RFP ZT-40M experiment has an Inconel bellows-type liner (dimensions R/a = 1.14 m/0.198 m) located inside an aluminum shell. External toroidal and poloidal windings drive the plasma currents. Iron transformer cores couple the primary and secondary toroidal currents. The electrical circuits allow, by a simple reconnection of the windings, nominal toroidal current risetimes of 0.25, 0.75, and 1.50 ms. Peak toroidal currents used in this study were $\leq$ 180 kA. To limit the number of variables in this study the current waveforms of the toroidal and poloidal circuits were adjusted to differ only by a time-scale factor.

The toroidal field reversal at the wall was kept small, -20 to -40 mT, with the ratio of the poloidal field at the wall to the mean toroidal field, $\theta = B_p(a)/\langle B_\phi \rangle$, held approximately constant at $\sim$ 1.5 at peak toroidal current. In addition the toroidal current was initiated near the zero of the poloidal voltage.

III. DIAGNOSTIC TECHNIQUES

Measurements of voltages, currents, magnetic fields, and fluxes were monitored on each discharge. The electrical behaviors of the discharge, including energy input, energy loss, and toroidal V·s consumption, have all been computed at the inside surface of the liner. The magnetic field profiles are assumed to be given by a Modified Bessel Function (MBF) model with $\mu = j(r)/B(r)$ = a constant in the inner 70% of the plasma radius, r; r falls smoothly to zero in the outer region.[2]

Electron density measurements were made using eight-chord CO_2-laser interferometry[3] and, on axis, by single-point ruby-laser Thomson scattering.[4] The eight chords of the interferometer allow a radial density profile to be derived including the central density, n_o, the width at half-maximum, w, and

the volume-averaged density, $\bar{n}$. The central chord average density, $\bar{n}_c$, is also obtained.

The radiated energy, E_{rad}, from the plasma was mainly determined by a platinum foil bolometer with a ~ 0.4-ms response time.[5] Further radiation data were provided by a number of spectrometers which looked along plasma diameters. In addition an array of six monochrometers directed along vertical chords of ZT-40M provided spatial distributions.[6] The spectrometer data yield signals which are functions of electron temperature and impurity concentration.

The electron temperature was measured by Thomson scattering on axis. Also, ultrasoft x-ray emission[7] along a vertical minor diameter of the discharge was detected by a dual-foil scintillator photomultiplier-type instrument. Beryllium foils 0.125 and 0.475 mm thick minimized unwanted effects of impurity and runaway radiation.

IV. OPERATING "WINDOW"

With each risetime the operating "window" for RFP formation was established by scanning the fill pressure, with the toroidal bias field adjusted to give matched-mode operation (self-reversal of the toroidal field is matched at the liner; no toroidal field change of this type occurs during the formation phase) and the field programming is set to give a $\theta \simeq 1.5$. A useful criterion for optimizing the RFP is the V•s consumption of the toroidal electric field up to the time of peak toroidal current, divided by the peak current, $I_{\phi p}$. The results for 0.25- and 0.75-ms risetimes are shown in Fig. 1 with peak toroidal currents of ~ 180 kA. The V•s consumption versus pressure for 0.25-ms risetime is relatively flat; that for the 0.75-ms risetime is larger and increases at both high and low pressures. The large scatter in the data is due to a "hysteresis" effect seen when the discharge conditions are changed. Several discharges are then necessary to establish a new equilibrium. In this study, time limited the number of discharges and all the data taken are presented in the figure.

As the fill density, n_{FILL}, is raised, the fraction of radiated energy E_{rad}/E_{in} (E_{in} is the energy input) increases, as in Fig. 2, for 180-kA discharges at the three risetimes, until a point is reached at which nearly all the energy input is lost to radiation.[1] The high fill-pressure side of the

RFP operating "window" is thus caused by increased radiation losses at the higher pressures and, as seen from Fig. 2, is insensitive to risetime.

The lower boundary to the operating fill-pressure range is characterized, frequently, by increased fluctuations in density and electrical noise and by gas breakdown limits for the 0.25- and 0.75-ms risetimes.

When the operating "window" with the 1.5-ms risetime was being determined, however, a new phenomenon was observed: at low filling pressures and/or high bias toroidal fields RFPs could not reliably be established. This behavior is demonstrated in Fig. 3. This figure compares as a function of time the toroidal current, I_ϕ; toroidal field at the wall, $B_\phi(a)$; average toroidal field, $\langle B_\phi \rangle$; and average central-chord electron density, $\bar{n}_c$, for two successive shots at p = 2.1 mtorr, which differed by only 4% in the toroidal bias field. At the lower bias field a conventional RFP is formed. At the higher bias field, however, the nonformation of an RFP discharge is signalled by departures of the I_ϕ, $B_\phi(a)$, and $\langle B_\phi \rangle$ waveforms from their respective RFP-formation signatures beginning at 0.5 ms. This is characterized by a drop in I_ϕ, the nonreversal of $B_\phi(a)$, and a drop in $\langle B_\phi \rangle$. In addition, $\bar{n}_c$, which is dropping rapidly for both cases, continues to drop to very low values after the nonformation of the RFP has been signalled.

Prior to the signalling of the RFP nonformation, the density is lower on the average for discharges that do not form an RFP. This is shown in Fig. 4 by plotting central chord density, $\bar{n}_{cp}$, measured at a time just prior to when the RFP nonformation would be signalled by the other diagnostics (i.e., looking only at the other diagnostics at this time there would be no way to tell whether the RFP was going to form or not); $\bar{n}_{cp}$ is plotted versus pressure for a representative group of shots at 180 kA and 1.5-ms risetime. The data on this figure suggest that there is a critical density, $\simeq 2 \times 10^{19}$ m^{-3}, below which RFP formation does not take place reliably. Furthermore, as shown in Fig. 5, when the bias field is increased at a fixed pressure, the density $\bar{n}_{cp}$ decreases. Thus, it may be a combination of the inverse dependence of $\bar{n}_{cp}$ on the bias field and a low-density limit for RFP formation that leads to the observed inability to form the RFP at a given pressure and high bias fields. It can also be seen from Fig. 5 that $\bar{n}_{cp}$ increases with increasing fill pressure at a fixed bias, which would explain why RFP discharges can be formed at higher biases at the higher pressures.

This type of RFP nonformation was not observed at the shorter risetimes, perhaps because the density has insufficient time to drop before reversal is achieved. Figure 6 shows that the $\bar{n}_c$ values for equivalent discharge conditions (peak toroidal current, toroidal bias field, and fill pressure) at the time of field reversal do indeed decrease as the risetime is increased.

The dependence of the boundary between "RFP/no RFP formation" seen with the 1.5-ms risetime on the filling gas pressures and bias toroidal field is shown in Fig. 7. Two peak toroidal currents, ~ 90 kA and ~ 180 kA, were investigated in some detail and the results with both currents are included in the figure. As mentioned earlier there is a hysteresis effect and the boundary is ill-defined.

V. VOLT-SECOND CONSUMPTION

The toroidal V•s input up to the time of peak current for the three risetimes was determined from the toroidal voltage. In Fig. 8 the input V•s per ampere is shown as a function of risetime for peak discharge currents of ~ 180 kA. The data can be fitted with a linear relationship for risetimes up to 1.9 ms by

$$\int V_\phi \, dt/I_{\phi_p} = (1.51 + 0.78 \, \tau_r)10^{-6} \text{ V•s/A} \quad , \tag{1}$$

with the risetime, τ_r, in ms. The first term on the right-hand side, 1.51×10^{-6}, is the toroidal current inductance (in henries) which is predicted by the MBF model[2] to be $L_\phi \simeq (\theta - 0.05)\mu H$ for ZT-40M (major radius = 1.14 m). With $\theta \simeq 1.53$ in the experiments, the calculated inductance of 1.48 μH agrees well with the 1.51×10^{-6} in Eq. (1). The second term is the V•s/A needed to drive the discharge resistance. The linear rise of the V•s/A with τ_r suggests that the variation of discharge resistance with time for the three risetimes is similar. An effective resistance, R_{eff}, can then be defined which when multiplied by the risetime gives the V•s/A needed because of the discharge resistance. According to theory, R_{eff} is a function of θ, which includes a screw-up factor,[8] and the peak discharge current. The observed dependence of R_{eff} on peak toroidal current is shown in Fig. 9 (θ kept almost constant) for the three risetimes. As the current increases R_{eff} drops, as would be

expected for classical resistivity if the temperature is higher at the higher currents. For the 1.5-ms risetime the data show that R_{eff} (neglecting the possible dependence on fill density) drops with current as

$$R_{eff} = 16.8 \times 10^{-3} \, I_{\phi_p}^{-0.64} \, \Omega \quad , \tag{2}$$

with I_{ϕ_p} in kA.

Using Eq. (2), which has only been established over a limited range of I_{ϕ_p}, the V•s input required to drive the discharge resistance in larger experiments can be estimated. Of particular interest at this time is a scaled-up ZT-40M (ZT-H) which has a minor radius of 0.40 m, major radius of 2.15 m, discharge current of 2×10^6A, and current risetime of 10 ms. We define an average resistivity, η_{aver}, which is given by

$$\eta_{aver} = R_{eff}^{M} \frac{A^M}{2\pi R^M}$$

$$\simeq 16.8 \times 10^{-3} \frac{A^M}{2\pi R^M} \left(I_\phi{}^M\right)^{-0.64} \quad ,$$

where the superscript M refers to the ZT-40M experiment and A and R are the cross-sectional area and major radius, respectively. Assuming that for equal current densities in ZT-H, i.e., $I_{\phi_p}{}^H = (A^H/A^M) I_{\phi_p}{}^M$, the discharge has the same average resistivity, we have

$$R_{eff}{}^H = \eta_{aver} 2\pi R^H / A^H$$

$$\simeq 16.8 \times 10^{-3} (A^M/A^H)^{0.36} (R^H/R^M) (I_{\phi_p}{}^H)^{-0.64} \quad ,$$

with the superscript H referring to the ZT-H experiment.

The effective resistance of ZT-H will then be 0.148 mΩ (using $a = 0.2$ m and $R = 1.14$ m for ZT-40M) at a discharge current level of 2 MA. The V•s consumption of ZT-H in resistive losses is then estimated to be 2.96 V•s for a

risetime of 10.0 ms. The poloidal flux input, $L_\phi I_\phi$, using the MBF model,[2] $\theta = 1.53$, and correcting for the larger major radius, is 5.5 V•s. The total V•s consumption for ZT-H is the sum of the two terms and for a risetime of 10.0 ms and 2.0 MA requires 8.4 V•s. A 20.0-ms risetime requires 11.4 V•s. This requirement can be met in preliminary designs of the experiment.

VI. ENERGY INPUT AND LOSSES

The total energy input to the discharge is calculated from the Poynting vector for toroidal and poloidal electric fields on the inside of the Inconel liner. The results are shown in Fig. 10 for discharge currents $\simeq$ 170-180 kA and the three risetimes. The spread of the data for the nominal 0.75-ms risetime allows at least two curves to be drawn through the data (the indicated errors are the root-mean-square square average duration of individual discharges), as can be seen in Fig. 10a,

$$E_{in}/I_\phi^2 = (1.06 \times 0.53\ \tau_r)10^{-6}\ J/A^2 \quad ,$$

or in Fig. 10b,

$$E_{in}/I_\phi^2 = (0.81 + 1.32\ \tau_r - 0.38\ \tau_r^2)10^{-6}\ J/A^2 \quad ,$$

with τ_r in ms. The chi-square goodness of best fit to the data is 0.24 for the linear rise and 0.14 for the quadratic. Further data are necessary to establish which of these two curves should be used to extrapolate to longer risetimes.

The energy lost by the discharge up to the time of peak toroidal current is calculated by (a) neglecting the plasma energy and (b) subtracting from the energy input the total magnetic field energy of the poloidal and toroidal fields (given by the MBF model[2]). The ratio of energy loss to energy input for peak discharge currents ~ 170-180 kA is shown as a function of risetime in Fig. 11. The straight line in the figure is the best fit to the data and has the form

$$(E_{loss}/(E_{input}) = 0.14 + 0.24\ \tau_r\ J/A^2,$$

with τ_r in ms. These data show that with risetimes of 0.25, 0.75 and 1.5 ms the energy loss is ~ 20, 30 and 50% of the energy input, respectively. (Clearly this relationship is only true for risetimes shorter than the ~ 1.5 ms examined in this study.)

With each risetime a series of discharges was made with different peak toroidal currents. In Fig. 12a is shown the input energy per ampere squared and in Fig. 12b, the energy loss per ampere squared. The equations for the best fit for a linear approximation follow:

0.25-ms risetime:

$$E_{in}/I_{\phi_p}{}^2 = (1.41 - 1.02 \times 10^{-6}\ I_{\phi_p})10^{-6}\ J/A^2 \quad ,$$

$$E_{loss}/I_{\phi_p}{}^2 = 0.31 \times 10^{-6}\ J/A^2 \quad ;$$

1.5-ms risetime:

$$E_{in}/I_{\phi_p}{}^2 = (2.53 - 4.04 \times 10^{-6}\ I_{\phi_p})10^{-6}\ J/A^2 \quad ,$$

$$E_{loss}/I_{\phi_p}{}^2 = (1.45 - 3.11 \times 10^{-6}\ I_{\phi_p})10^{-6}\ J/A^2 \quad ;$$

where I_{ϕ_p} is in amperes. In both figures the data show that as the discharge current increases both the energy input per amp-squared and the energy loss per amp-squared fall with toroidal current for the two risetimes. The decrease is larger for the longer risetimes.

VII. ELECTRON TEMPERATURE

The results of Thomson scattering time scans obtained under matched-mode discharge conditions are shown in Figs. 13 and 14. Figure 13 shows axial temperatures as functions of machine time for 180-kA discharges with risetimes of 0.25, 0.75, and 1.5 ms. The corresponding fill pressures are 1.6, 2.5, and

3.1 mtorr. The 0.25-ms risetime results were obtained 5 months earlier than the 0.75- and 1.5-ms results, and the 0.75- and 1.5-ms results were obtained within a few days' interval.

The axial electron temperatures reach a level of the order of 300 eV with all three risetimes. Uncertainties in reproducibility introduced during the time interval separating the 0.25 ms from the other measurements precludes a more precise conclusion on the risetime scaling of the temperature.

Figure 14 shows axial Thomson scattering temperatures as functions of time for optimized 1.5-ms risetime with 180-, 140-, and 100-kA discharges. The fill pressures are 3.1, 2.5, and 2 mtorr. The triangles are the data for 180-kA discharges already shown in Fig. 13. The data show that the maximum temperature increases with increasing peak current. Impurity burnthrough is achieved at all three current levels.

The Thomson scattering data have been compared with the ultrasoft x-ray data. An example of the ultrasoft x-ray results is shown in Fig. 15 for an optimized 180-kA, 0.75-ms risetime condition. The result is typical in that it produces a satisfactory agreement with Thomson scattering central temperatures up to approximately 3 ms machine time. Beyond this time, the ultrasoft x-ray temperature continues to rise, whereas the Thomson scattering data level off or start to decline. The discrepancy between the behavior of the two diagnostics has been tentatively attributed to radiation from heavy-metal impurities or runaway electrons.[9] (Note that the data reported here were taken before ZT-40M was modified to improve its operation.)

Typical time histories of D_β, OIV, and OVI, normalized to the appropriate chord electron densities, are shown in Figs. 16a and 17a for optimized 180-kA, 0.25-ms and 180-kA, 1.5-ms discharges, where the abscissae have been scaled to the respective current risetimes. Figures 16b and 17b show the total power radiated on the same time scales. Also shown in the figures are the central chord-averaged electron density and the toroidal discharge current. It is seen that the progression through various ionization stages of oxygen (indicative of increasing electron temperature) occurs in a similar time scale relative to the current risetime.

The time of peaking of emission of the various impurity lines gives a rough indication of the heating rate of the plasma. The machine time to peak emission of CV for 180-kA discharges with risetimes of 0.25, 0.75, and 1.5 ms is shown in Fig. 18 as a function of deuterium fill pressure. Optimized mode

fill pressures for these risetimes are 1.6, 2.2, and 3.1 mtorr. These data have not been normalized to the electron density. However, the time to peak emission increases, as expected, with fill pressure. A comparison with Thomson scattering, at the optimized fill pressure, gives ratios of CV excitation potential to axial Thomson scattering temperature at the time of peak emission which vary between 3.6 for the shortest risetime to 1.8 for the longest.

A plot of CV radiation intensity, at the time of peak emission, as a function of impact parameter (minor radius) is shown in Fig. 19 for optimized 180-kA discharges, with 0.25-, 0.75-, and 1.5-ms risetimes. The radial distributions of this radiation indicate effective heating ($\gtrsim$ 50 eV) throughout the observed discharge volume at all three risetimes.

The time behavior of the oxygen line radiation has been simulated by means of a zero-dimensional computer code. Inputs were the measured volume-averaged electron density and an assumed time dependence of the temperature. Using this information, the code solved the rate equations for the atomic species of interest.* The time dependencies of the temperatures were then varied until the calculated time histories of the oxygen lines best fit the data.

The results are shown in Fig. 20 for optimized 180-kA, 1.5-ms risetime discharges. The calculated temperatures are to be interpreted as volume-averaged temperatures, because volume-averaged densities and chord-averaged radiation measurements are used in the calculations. Thomson scattering results indicate axial electron temperatures of 80 eV at 0.65 ms. The agreement is satisfactory if a relatively flat temperature profile is assumed.

VIII. DENSITY BEHAVIOR

The electron density for the five optimized matched-mode discharges (see Table I for discharge conditions) exhibits certain qualitative similarities independent of peak current or risetime. These features are displayed in Figs. 21 and 22, where the toroidal current I_ϕ, the toroidal field at the wall $B_\phi(a)$, and volume-average density $\bar{n}$, are plotted for the 0.25- and

*R. B. Howell, P. G. Weber, and R. G. Watt, personal communication of unpublished data, Los Alamos document LA-UR-81-1376 (April, 1981), to be submitted for journal publication.

TABLE I - OPTIMIZED MATCHED MODE CONDITIONS

I_ϕ and B_ϕ Risetime (ms)	I_{MAX}(kA) (Nominal)	I_{MAX}(kA)	Fill Pressure (mtorr)
1.5	100	97	1.9
1.5	140	137	2.5
1.5	180	185	3.1
0.75	180	194	2.2
0.25	180	175	1.6

1.5-ms risetimes, respectively, for a nominal discharge current of 180 kA. The time interval displayed on the abscissa is scaled to the respective risetime. Also plotted in Figs. 21b and 22b is the half-width at half maximum, w, of the density profile. After the initiation of the discharge current the density rises rapidly to a peak value, $\bar{n}_{MAX}$, at time t_{nMAX}. Thereafter, it initially decays rapidly to a density $\bar{n}_p$ at a time t_{np}; and then it decays less rapidly, after showing a slight momentary increase. Note that with the faster risetimes the average density is higher with a narrower profile at peak current than with the longer risetimes.

The width w shows a general decrease with time with some oscillatory behavior superimposed. This oscillatory time behavior does not appear to scale with risetime. This may be the result of exchanges of particles between the wall and the outer parts of the plasma, since the oscillations of w are mainly due to oscillations in the plasma density in the outermost chords (near the wall) of the interferometer.

The time t_{np} at the end of the rapid density decrease occurs near to the time of field reversal at the wall, t_R, for each of the five cases (though the transition is less well defined at the 0.25- and 0.75-ms risetimes). This correlation is shown in Fig. 23 where t_{np} is plotted versus t_R. Since the time scale for the toroidal current is the same as for the toroidal field in the five optimized, matched-mode cases, this apparent correlation of t_{np} with t_R may be a correlation with some property of the toroidal current and/or voltage waveforms. However, the good agreement with the scaling of Fig. 23 of the data point for the mismatched (0.75 ms, B_ϕ; 1.50 ms, I_ϕ) risetimes,

indicates that it is a correlation of the density time with the field-reversal time, rather than with a toroidal current time, which is important.

The scaling of volume-averaged density, $\bar{n}$, with peak current is shown in Fig. 24 for the three optimized, matched-mode conditions at the 1.5-ms risetime. Both the peak density $\bar{n}_{MAX}$ and the density $\bar{n}(2.3)$, at 2.3 ms after the start of the current (well after the establishment of the RFP), show an approximately linear dependence on I_{MAX}. For the densities $\bar{n}_{MAX}$ and $\bar{n}(2.3)$ the corresponding values of the parameter $I_{MAX}/\pi a^2\bar{n}$ are $\sim 10^{-14}$ Amp-m and $\sim 10^{-13}$ Amp-m. By contrast, the value of density $\bar{n}_p$ at the end of the rapid density loss period is independent of I_{MAX}. As a fraction of the fill density, the peak density increases weakly from 50 to 70% as the current is increased, but the density fraction of $\bar{n}(2.3)$ is in the 6 to 7% range, independent of current.

The behaviors of the densities $\bar{n}_{MAX}$, $\bar{n}_p$, and $\bar{n}(2.3)$ as functions of risetime are shown in Fig. 25, for optimized matched-mode operation at 180-kA peak current. The peak density $\bar{n}_{MAX}$ increases with risetime and maintains approximately a constant fraction of 70% of the fill density. The density $\bar{n}_p$ shows little or no dependence on risetime. As a consequence, the density lost during the rapid-loss period, $\bar{n}_{MAX} - \bar{n}_p$, increases strongly with risetime. As a percentage of the fill density, however, $\bar{n}_{MAX} - \bar{n}_p$ increases only moderately, from about 40% at the 0.25- and 0.75-ms risetimes to about 60% at the 1.5-ms risetime. The density $\bar{n}(2.3)$ shows no dependence on risetime, which leads to a value of

$$\frac{I_{MAX}}{\pi a^2 \bar{n}(2.3)} \simeq 10^{-13} \text{ A-m} ,$$

independent of the risetime, the same value as in the current scaling study. Stated another way, a greater fraction of the fill density is lost in establishing the RFP discharge at longer risetimes for the optimized matched mode conditions presented here.

The corresponding scaling of the time dependence of the volume-average density with risetime has been indicated in Figs. 21 and 22: as the risetime is increased the time t_{nMAX} at peak density increases only slightly while the

time t_{np} at the end of the rapid density-loss period increases strongly. This leads to an approximately linear dependence on risetime of the duration of rapid density loss, $t_{np} - t_{nMAX}$. (This result also follows from Fig. 23 and its discussion.) Combined with the results in the preceding paragraph this result yields a time rate of change of the average density during the rapid-loss period, $(\bar{n}_{MAX} - \bar{n}_p)/(t_{np} - t_{nMAX})$, that decreases only moderately, by about 40%, as the risetime is increased from 0.25 to 1.5 ms. Thus, the rate of density loss during the rapid-loss period is only a weak function of risetime, and the larger density losses at the longer risetimes apparently occur simply because the losses continue for longer times.

IX. RADIATION ENERGY LOSS

The total radiated energy emitted from the discharge is largest in the early phase of the discharge before the impurity states have burned through and when the electron density is high. A time t_{RAD} is defined, relative to the start of the toroidal current, at which this strong radiation phase is 63% complete. Figure 26 shows the ratio t_{RAD}/t_{IMAX}, where t_{IMAX} is the time of peak current, for the three risetimes with I_{MAX} = 180 kA as a function of pressure (for nonoptimized matched-mode conditions). The 0.25-ms risetime case differs markedly from the two longer risetimes in that t_{RAD} is greater than or equal to t_{IMAX} for pressures $p \geq 2.5$ mtorr. Thus, in determining the radiation losses at higher pressures for the 0.25-ms risetime, E_{RAD} is evaluated at the time $t \gtrsim t_{RAD}$ rather than $t = t_{IMAX}$ (see Fig. 2 and its caption).

For this same set of data E_{LOSS} up to the time $t = t_{RAD}$ is independent of the risetime at a given pressure, as shown in Fig. 27, indicating no significant changes of the total plasma-loss processes as the risetime is increased. (This result does not contradict the result of Fig. 11 since the Fig. 27 data are evaluated at $t = t_{RAD}$ and the Fig. 11 data at $t = t_{IMAX}$.) Furthermore, for the range of pressures, $p \simeq 1.7 - 3.2$ mtorr, corresponding to the optimized matched-mode conditions, this value of E_{LOSS} is nearly independent of pressure. It can also be shown that the burnthrough of individual impurity states occurs at approximately the same value of E_{LOSS} independent of risetime for optimized, matched-mode conditions. The lack of dependence of $E_{LOSS}(t_{RAD})$ on risetime or pressure over this range of

parameters suggests that a definite amount of energy is required to establish the RFP discharge.

As already noted with Fig. 2, the input energy fraction that is radiated during start-up at a given pressure is not a sensitive function of risetime duration. As also observed, this radiated fraction increases with increasing fill density. Thus, the higher radiation losses at the longer risetimes occur because it is necessary to operate at higher fill densities in order to avoid the density starvation effect discussed in Sec. III and to minimize the V•s/A consumption.

We have investigated whether the increased radiation fraction at longer risetimes (and the accompanying higher fill pressures for optimized conditions) is related to an increase in impurity content generated by, for example, an increase in the time of wall contact. By normalizing the line intensities of various oxygen lines to the line-averaged electron density (Figs. 16a and 17a) with time scales normalized to the risetime, we find that the behavior of the signals is essentially independent of the risetime, suggesting that the concentration of the major impurity, oxygen, does not change appreciably. This may indicate that the increased radiation fraction at higher fill densities is due mainly to higher electron densities.

Plots of neutral nickel and chromium line radiation (scaled similarly to Figs. 16a and 17a) show the same time behavior for all risetimes, including enhanced emission just prior to the time of field reversal, indicating increased wall interactions at that time. The electron density normalized intensities for the metal lines do increase somewhat with risetime during start-up, suggesting more wall interaction at longer risetimes. However, after the set-up phase, there appears to be no significant overall difference in the radiated power levels for the various risetimes, so that the increased interaction time does not appear to be detrimental to the resultant RFP plasma.

The total radiated power, P_{RAD}, as measured by the bolometer, follows rather closely the time dependence of the electron density for all risetimes. Smoothed fits to the bolometer data, corrected for the bolometer time response, are shown for comparison in Figs. 16b and 17b. This correlation leads us to conclude that the predominant radiation energy losses during the start-up are strongly influenced by the instantaneous electron density, and are not primarily due to the specific oxygen ionization states.

As is also seen from Figs. 16b and 17b, a significant portion of the bolometer radiation losses are complete by the time of reversal of the toroidal field at the wall, $B_\phi(a)$.

The ratio E_{RAD}/E_{IN}, up to the time of peak current, is plotted in Fig. 28 for the five optimized, matched-mode conditions versus $\pi a^2 n_{FILL} / I_{MAX}$. The data points for the three different currents at the 1.5-ms risetime appear to lie on a curve similar to the 180-kA data presented in Fig. 2. This result indicates that the variable $\pi a^2 n_{FILL}/I_{MAX}$ is useful for predicting radiation at different currents, densities, and risetimes (a result previously established on the ETA-BETA II experiment[10] for a single risetime).

X. SUMMARY OF EXPERIMENTAL OBSERVATIONS

The behavior of ZT-40M at longer risetimes is characterized as follows.

- Operation at longer risetimes, optimized in terms of flux consumption, density pumpout and fluctuations, is at higher fill pressures than for shorter risetimes. This leads to larger radiative losses, a larger V•s/A consumption, and a larger fraction of the energy input being lost for the longer risetimes.
- The V•s/A consumption is found to rise linearly with risetime for constant current. Extrapolation to the proposed ZT-H experiment indicates the V•s requirement is met in preliminary designs.
- The early, very rapid density pumpout ends near the time the toroidal field reverses. Reversal of the toroidal field at the wall plays an important role in the density loss rate.
- There is a critical low-density limit at the time of field reversal below which RFP formation is unreliable. This fact, coupled with the observed inverse dependence of density on bias field, is suggestive that a density starvation process determines the observed high bias field limit for RFP formation in the 1.5-ms-risetime case. Also, for a given bias field and fill density, the density is higher at the shorter risetimes, which may explain why the low-density limit was observed only at the 1.5-ms risetime.

- For optimized interval matched-mode discharges, the time duration of the rapid density loss period scales linearly with risetime at constant current and is nearly independent of current for the 1.5-ms risetime. The density $\bar{n}_p (\simeq 3 \times 10^{19}\ m^{-3})$ at the end of this period is nearly independent of current and risetime. At the longer risetimes of ZT-H neutral gas puffing during the start-up phase will therefore be indicated.
- The values of $I_{max}/\pi a^2 \bar{n}_{max}$ are $\sim 10^{-14}$ A/m independent of current at the 1.5-ms risetime and increase to $\sim 2 \times 10^{-14}$ A/m for 180 kA discharges at the 0.25-ms risetime. (This difference may be related to the fact that the time to peak density at 0.25 ms is about one-half that at the 1.5-ms risetime).
- With peak discharge currents of ~ 180 kA the axial electron temperatures reach ~ 300 eV with all risetimes.
- As a function of peak discharge current at the 1.5-ms risetime the maximum temperature increases with current. Oxygen impurity burnthrough is achieved with currents $\gtrsim$ 100 kA.
- The temperatures suggested from the ultrasoft x-ray data are in satisfactory agreement with Thomson scattering axial temperatures up to 3 ms machine time. The discrepancy found at later times (the ultrasoft x-ray temperatures are higher than those from the Thomson scattering method) is attributed to radiation from heavy-metal impurity radiation or runaway electrons.
- Plasma impurity content does not appear to be a strong function of the risetimes examined and radiation levels in the RFP discharge after start-up are essentially independent of the start-up phase. The major radiation losses for matched-mode operation occur prior to reversal of the toroidal magnetic field and formation of the RFP configuration.

XI. DISCUSSION

The results of this study on the V•s consumption in the formation phase support the work on other experiments.[11-12,*] There is general agreement that

*Private communications from A. A. Newton and E. P. Butt; Y. Hirano and A. A. Newton; and T. Tamano.

the V•s/A consumption increases with risetime and decreases with peak toroidal current. Comparison of the V • s/A used in the different experiments, however, is difficult in that the physical sizes and toroidal currents are different. In addition there are only limited data for matched-mode of operation from other experiments with which to compare those from ZT-40M which are exclusively, in this report, matched-mode operation. After an examination of available data we find it unprofitable at this time to attempt meaningful correlations between the four experiments now operating. The data are incomplete.

We suggest that investigations on the different experiments be directed to obtaining the following information.

- Determine the discharge poloidal inductance as a function of θ by extrapolating the V•s/A consumption with different risetimes to zero risetime. The inductance determinations would allow us to choose the optimum MBF model for describing the magnetic field distributions in RFP experiments.
- Determine R_{eff} as a function of discharge current with different risetimes. The data would be useful in comparing different experiments with the same current densities. A minor-radius scaling relation would be determined. The impurity content in the different experiments, unfortunately, will make the interpretation difficult, especially during start-up.
- A comparison of aided and self-reversed modes of operation would give the additional V•s/A consumption needed in the self-reversed mode and allow comparisons among all four experiments. (OHTE with a B_ϕ flux conserving shell can only be operated in the self-reversed mode.)

The above data could result in a set of scaling relationships between the present experiments with which the operation of future machines could be predicted.

The low-density limit as found in ETA-BETA II due to increased magnetic fluctuations[11] was not as well defined in ZT-40M. With the long risetimes (1.5 ms) in ZT-40M, the low fill density limit arose because the reversal of the field at the wall did not occur. At the shorter risetimes the low fill density limit was characterized, frequently but not always, by increased magnetic fluctuations or hard (250-keV) x-ray production and by gas-breakdown limits.

ACKNOWLEDGMENTS

The authors thank A. R. Jacobson for the use of the data from his eight-chord interferometer. The assistance of the ZT-40M team was invaluable in obtaining the data and running the experiment. We also thank J. N. DiMarco, W. E. Quinn and H. Dreicer for their support.

REFERENCES

1. D. A. Baker, et al., Proc. 9th Int. Conf. Plasma and Controlled Fusion Research, Baltimore, Maryland, September 1-8, 1982, Paper CN-41/H-2-1.

2. K. F. Schoenberg, R. F. Gribble and J. A. Phillips, Nucl. Fusion 22 (1982).

3. A. R. Jacobson, Rev. Sci. Instrum. 49, 673 (1982).

4. D. A. Baker et al., "Four Feedplate Operation of ZT-40 With Passive Crowbars", Los Alamos National Laboratory report LA-8752-MS (January 1982).

5. G. Miller, J. C. Ingraham, and L. C. Schrank, Rev. Sci. Instrum. 53, 1410 (1982); also J. C. Ingraham and G. Miller, Los Alamos National Laboratory report LA-9352-MS (May 1982).

6. R. G. Watt, Los Alamos National Laboratory report LA-8823-MS (May 1981).

7. R. G. Watt, E. M. Little, and K. S. Thomas, Bull. Amer. Phys. Soc. 27, 8, 1108 (1982).

8. D. J. Lees and M. G. Rusbridge, Proc. 4th Int. Conf. Ionization in Gases 2, 954, Uppsala, August 17-21, 1959 (North Holland Publishing Co., Amsterdam, 1960).

9. R. G. Watt, E. M. Little, and K. S. Thomas, Los Alamos National Laboratory report LA-9588-MS (December 1982).

10. S. Costa, R. De Angelis, S. Ortolani, and M. Puiatti, Univ. Padua report UPee 82/03 (1982).

11. A. Buffa, S. Costa, R. De Angelis, L. Giudicotti, C. W. Gowers, et al., Proc. 8th Int. Conf. Plasma Physics and Controlled Fusion Research, Brussels, 1980, IAEA Vienna, Vol. 2, 275 (1981).

12. A. Buffa and S. Ortolani, Proc. Eur. Phys. Conf., Moscow, L-173/P (September 1981).

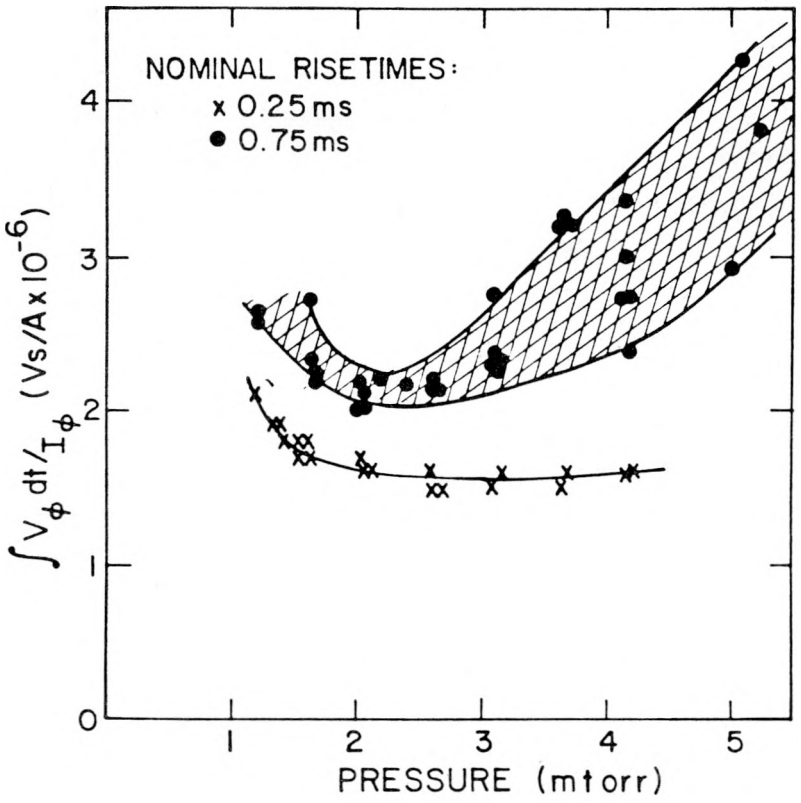

Fig. 1.
The V·s/A consumption versus filling pressure for 0.25- and 0.75-ms current risetimes. The spread in the data is due to a hysteresis effect when the initial conditions are changed.

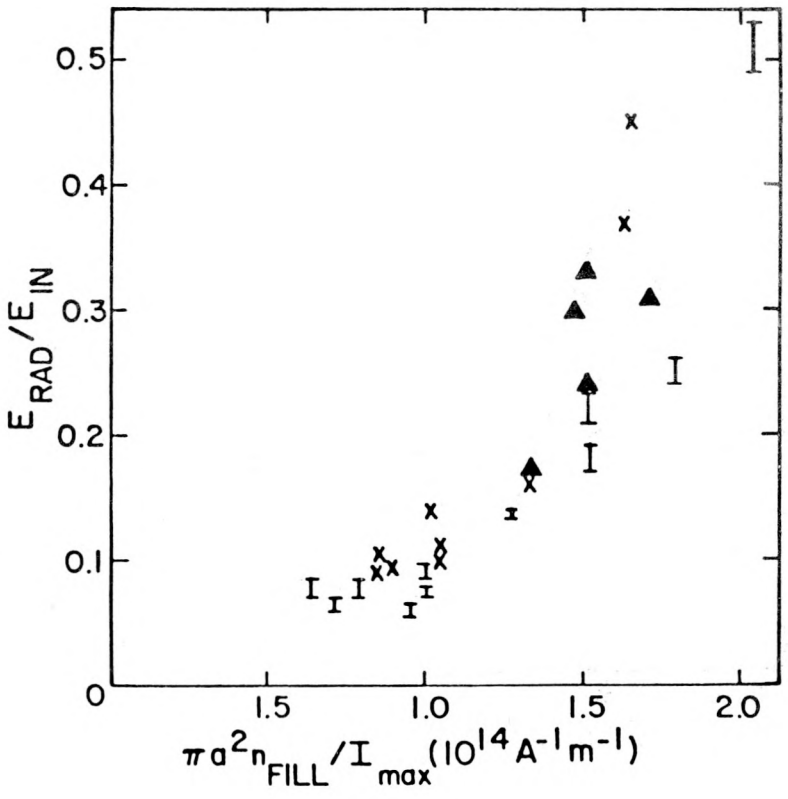

Fig. 2.
E_{RAD}/E_{IN} versus $\pi a^2 n_{FILL}/I_{MAX}$ for 1.5- (Δ), 0.75- (x), and 0.25-ms (I) risetimes, evaluated up to the time of peak toroidal current I_{MAX} for the 1.5- and 0.75-ms risetimes, and up to a time (shortly after peak current) when the radiation phase of start-up is complete for the 0.25-ms risetime. (a = minor radius = 0.20 m, n_{FILL} = fill density, and I_{MAX} = peak toroidal current.)

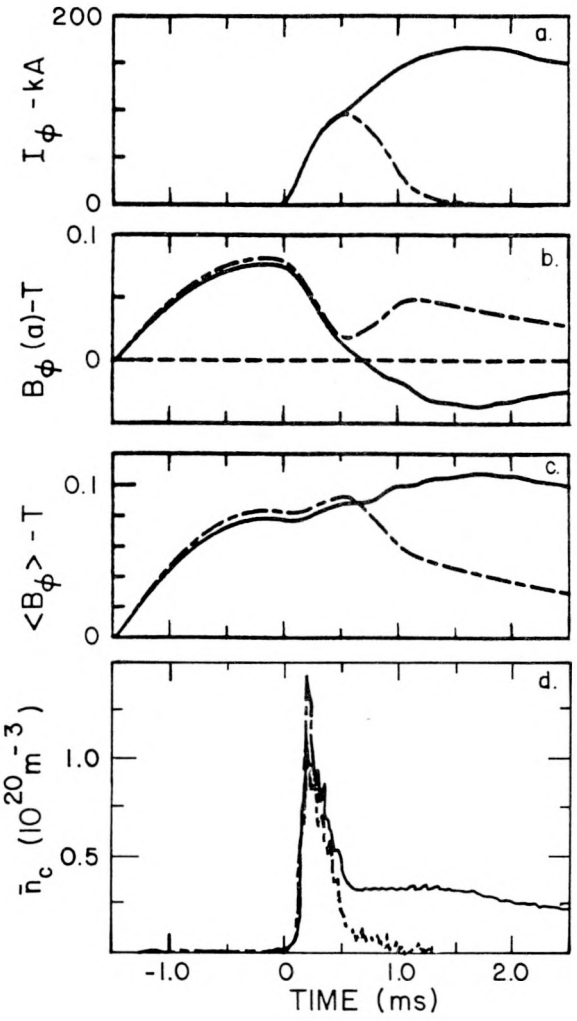

Fig. 3.

Toroidal current I_ϕ, toroidal field at the wall $B_\phi(a)$, average toroidal field $\langle B_\phi \rangle$, and average central chord density $\bar{n}_c$ as a function of time for two discharges with different toroidal bias fields. Solid line, bias field = 0.077 T; dashed line, bias field = 0.080 T.

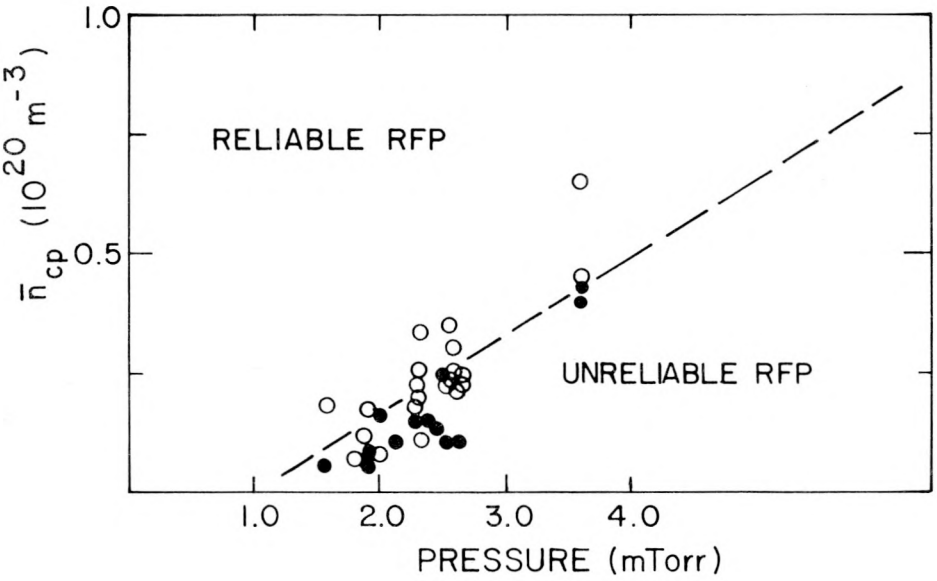

Fig. 4.

Central chord-averaged density $\bar{n}_{cp}$, just prior to the point at which the signaling of RFP nonformation would occur on other diagnostics, as a function of pressure. Open circles = RFP formation; darkened circles = no RFP formation.

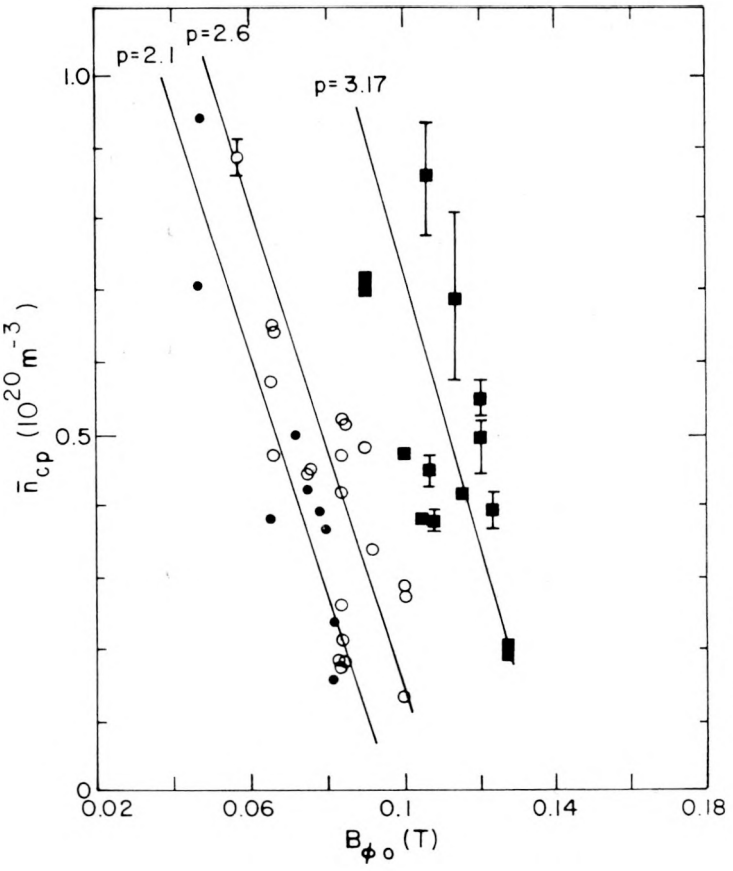

Fig. 5.

Central chord-averaged density $\bar{n}_{cp}$, just prior to the point at which the signaling of RFP nonformation would occur on other diagnostics, as a function of bias field $B_{\phi o}$, for three operating pressures: p = 2.1 mtorr (●), p = 2.6 mtorr (o), and p = 3.1 mtorr ([]). Error bars, shown where a data point is the average of several shots, represent the scatter of the data about the mean.

Fig. 6.

Central chord-averaged density $\bar{n}_c$ as a function of risetime for constant discharge conditions. Density is measured at the time of field reversal for all cases since the RFP was formed for all cases shown. Error bars used where a data point represents an average of several discharges represent the scatter about the mean. Peak current = 180 kA for all cases. Other conditions: $B_{\phi o}$ = 0.12 T, p = 3.7-4.1 mtorr (●); $B_{\phi o}$ = 0.10 T, p = 3.0 mtorr (Δ); $B_{\phi o}$ = 0.10 T, p = 1.6 mtorr ([]).

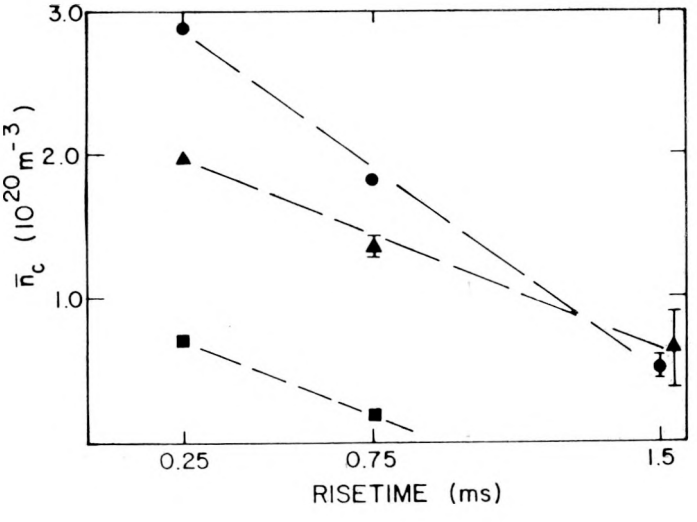

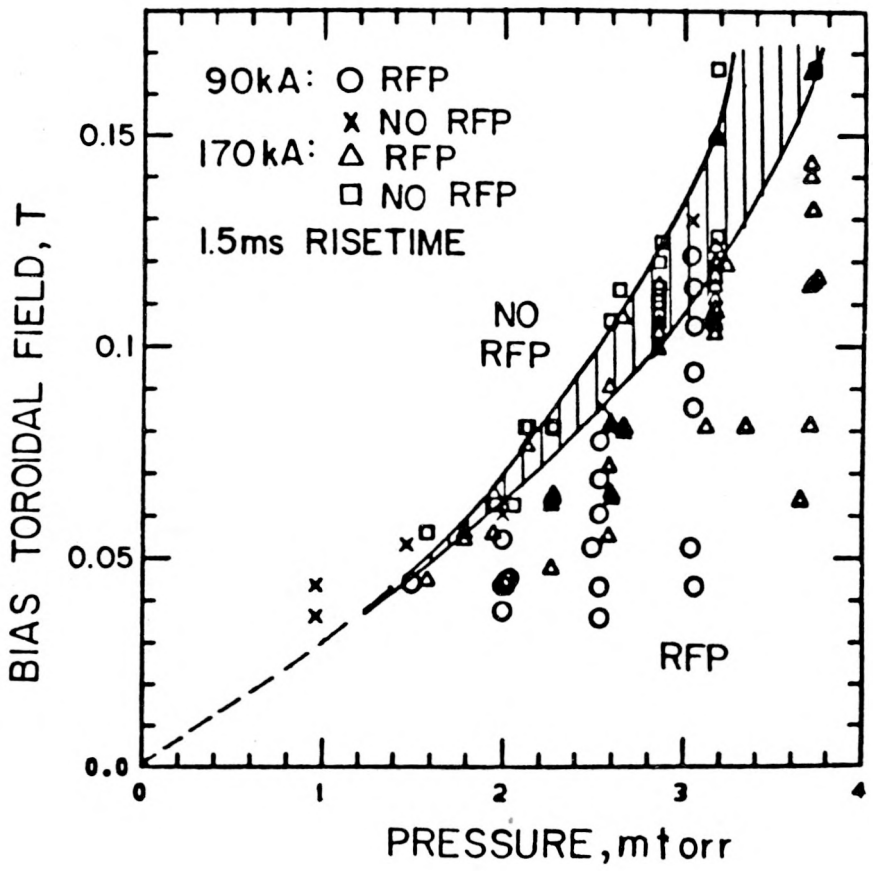

Fig. 7.

The boundary in filling pressure and bias toridal field which defines "RFP/no RFP" formation; τ_r = 1.5 ms.

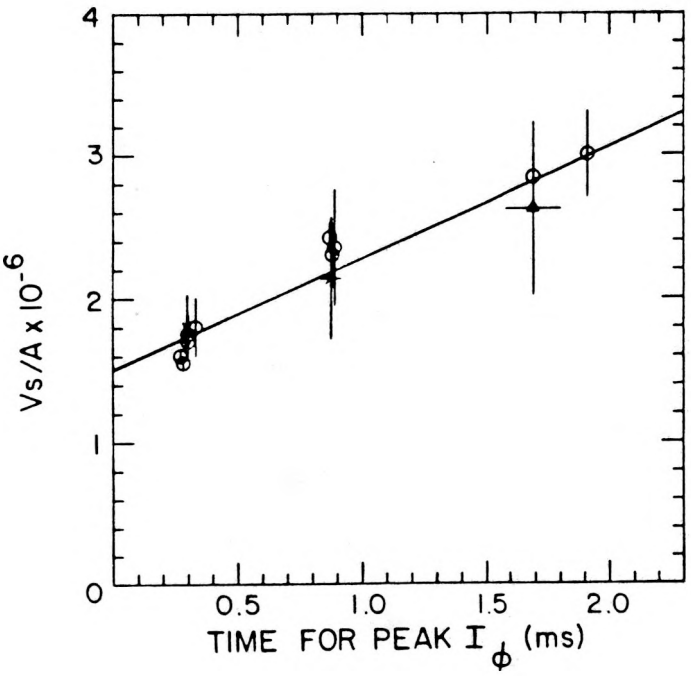

Fig. 8.

Input V·s/A at peak toroidal current as a function of time to peak current; peak toroidal current ~180 kA.

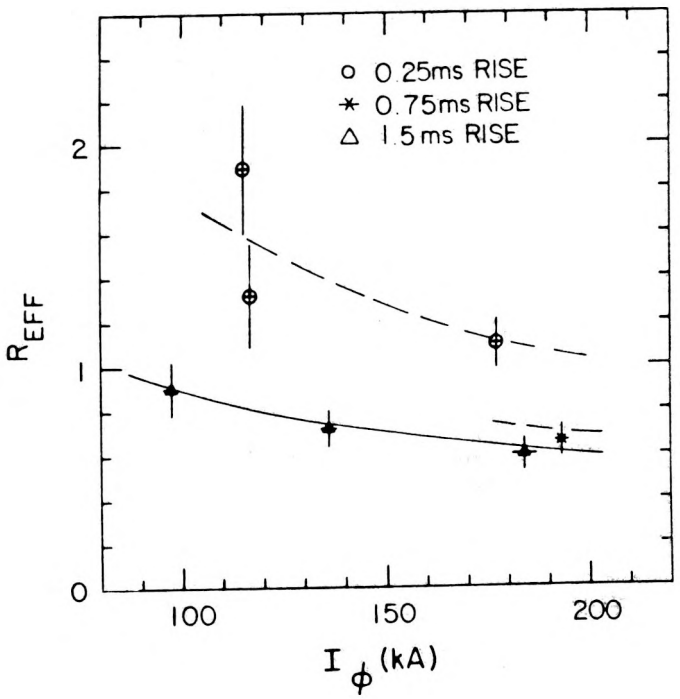

Fig. 9.

R_{eff} versus toroidal current for the three risetimes.

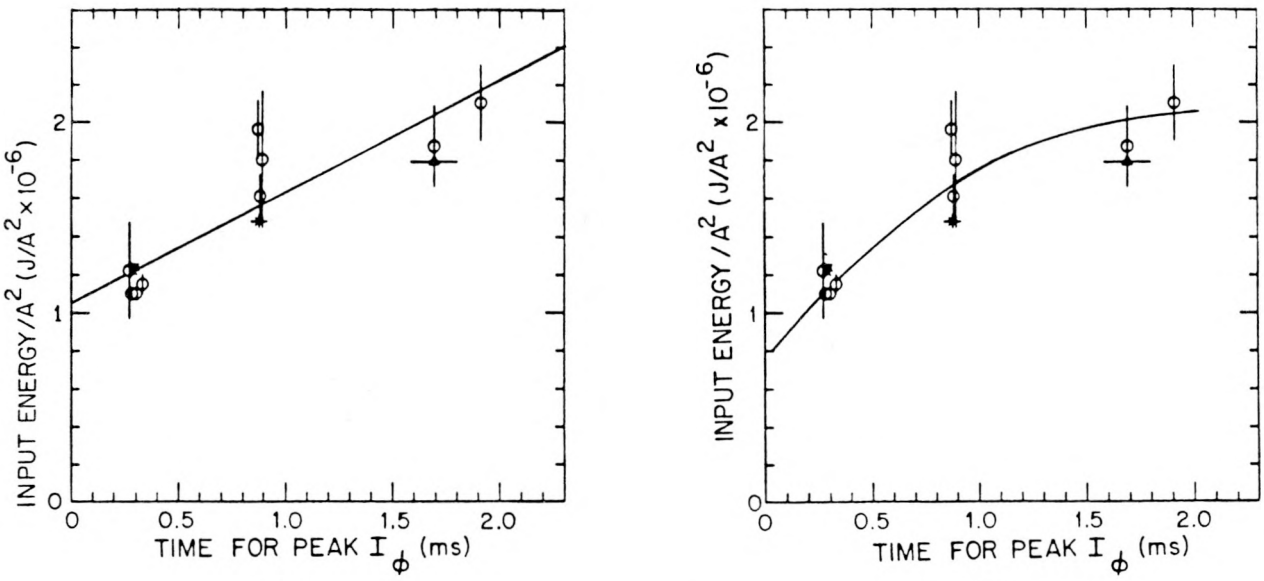

Fig. 10.

Energy input per current squared at peak current as a function of risetime; peak toroidal current ~180 kA. (a) Linear fit and (b) nonlinear fit.

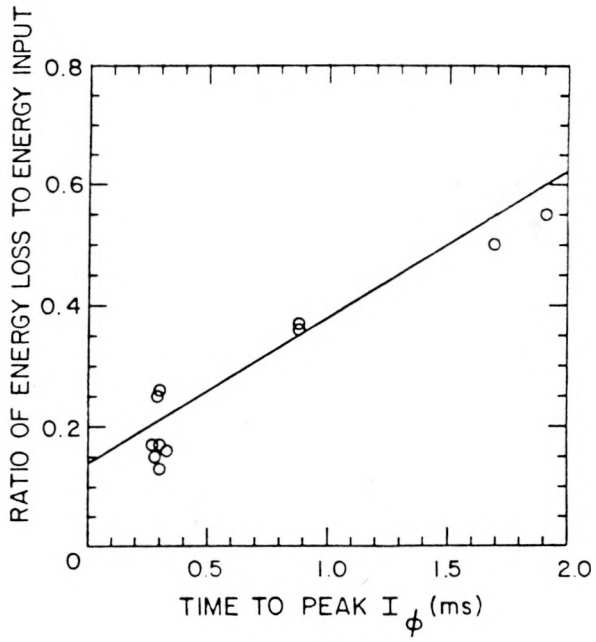

Fig. 11.

Ratio of energy loss to energy input as a function of toroidal-current risetime; peak toroidal current ~ 180 kA.

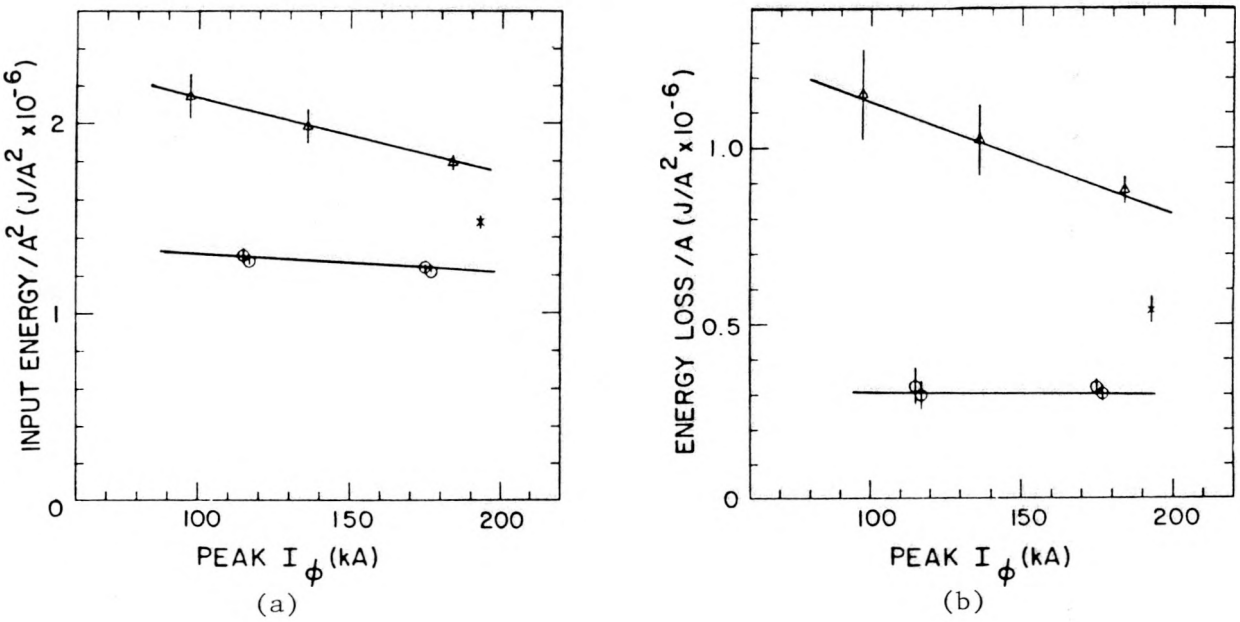

Fig. 12.

Input energy per current squared (a) and energy loss per current squared (b) versus peak toroidal current: τ_r = 0.25 ms (0), 0.75 ms (*) and 1.5 ms (Δ).

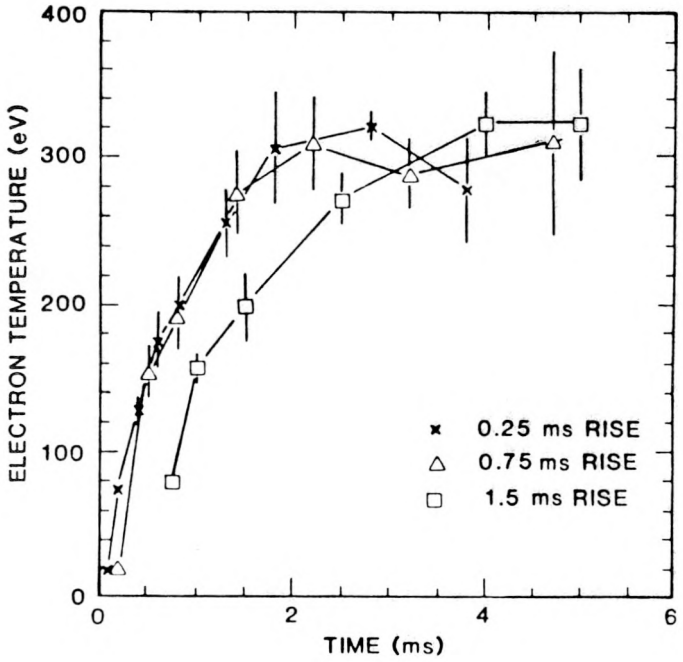

Fig. 13.

Axial electron temperatures from Thomson scattering data as a function of time with current risetimes of 0.25, 0.75, and 1.5 ms: toroidal current 180 kA.

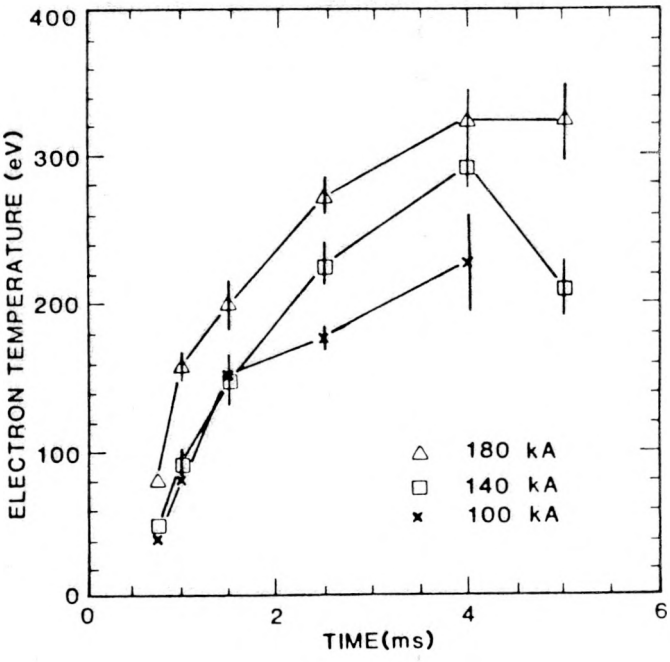

Fig. 14.

Axial Thomson scattering temperatures as a function of time for optimized 1.5-ms risetime. Toroidal current, 100, 140, and 180 kA.

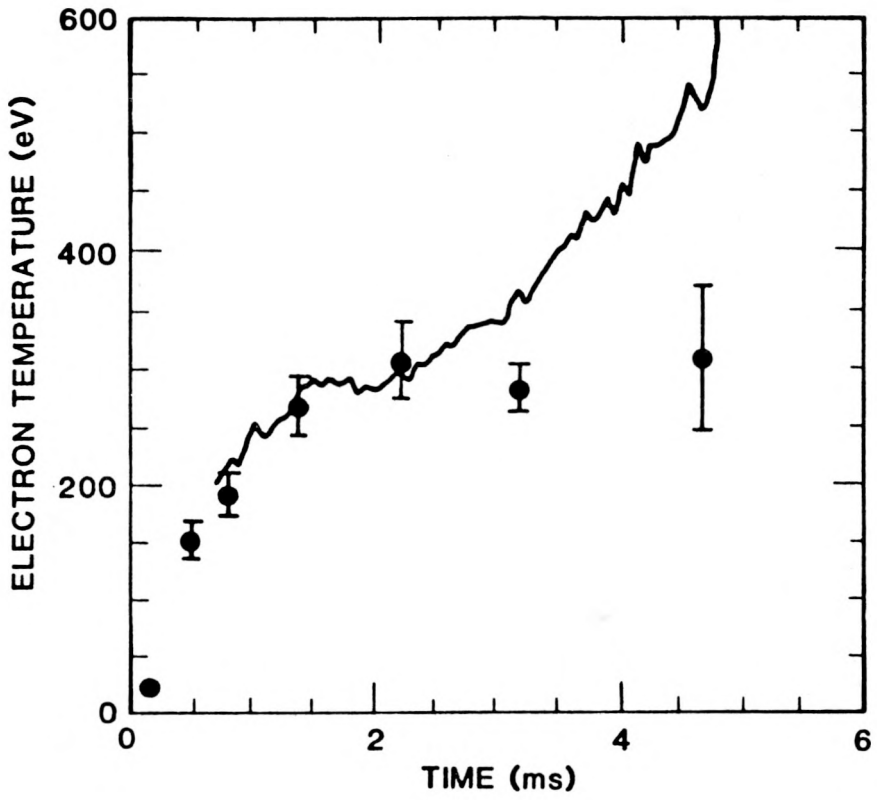

Fig. 15.

Comparison of the temperatures calculated from ultrasoft x-ray data and that from Thomson-scattering data: toroidal current ~ 180 kA, and τ_r = 0.75 ms.

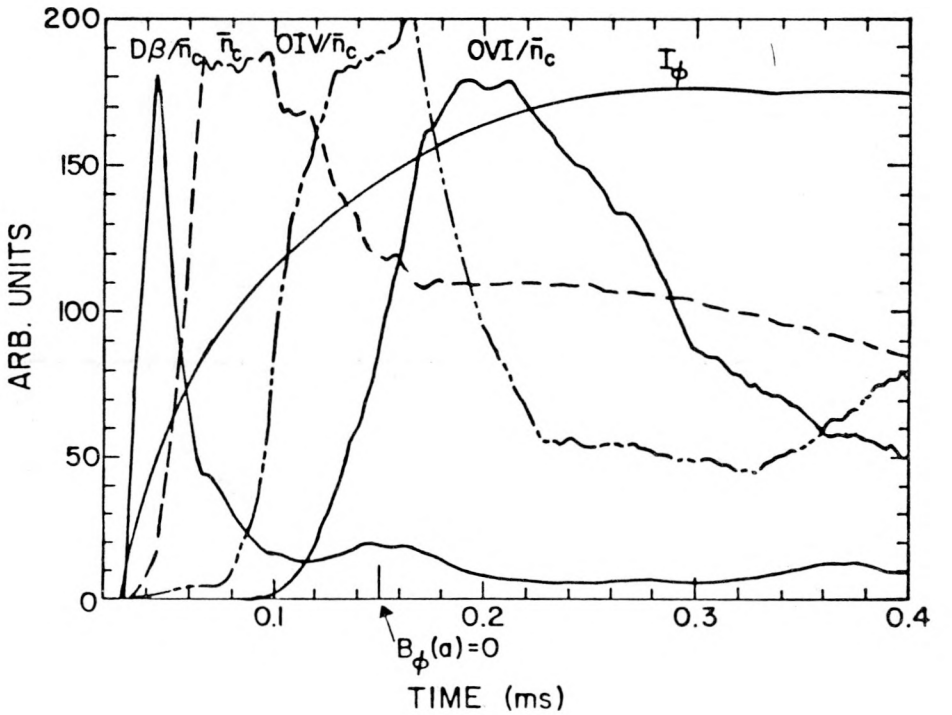

(a)

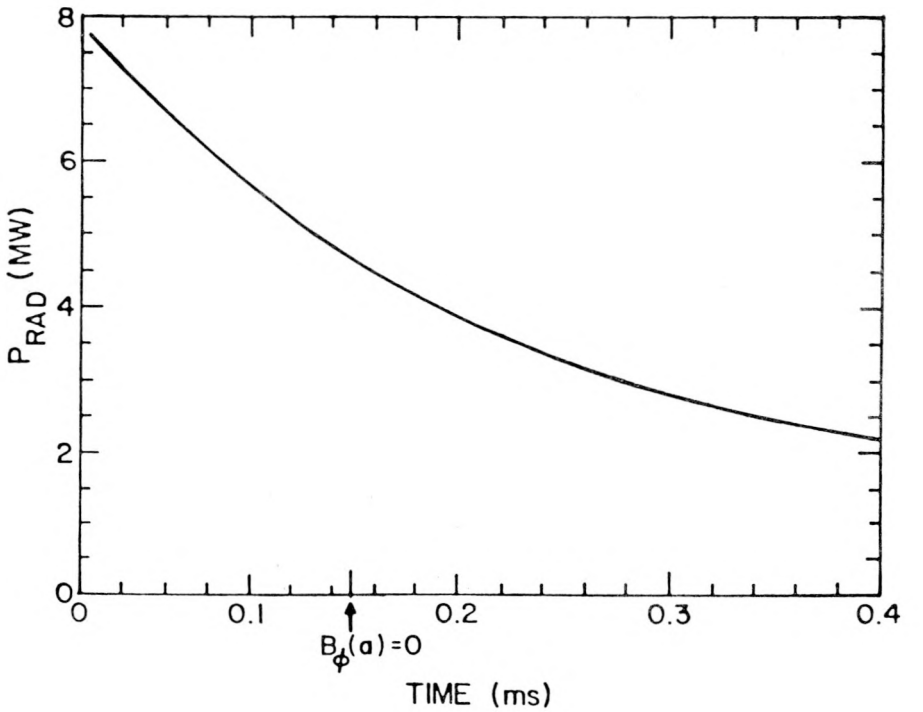

(b)

Fig. 16.

Data for 180-kA, 0.25-ms risetime case: (a) Plasma current I_ϕ, line average density $\bar{n}_c$, and normalized line radiation for D_β, OIV, and OVI during start-up. (b) Bolometer power P_{RAD} during start-up. Note that the apparent early start of P_{RAD} relative to the density for the 0.25-ms risetime is fictitious and appears to be due to a small systematic error introduced when correction for the 0.4-ms bolometer response time is made.

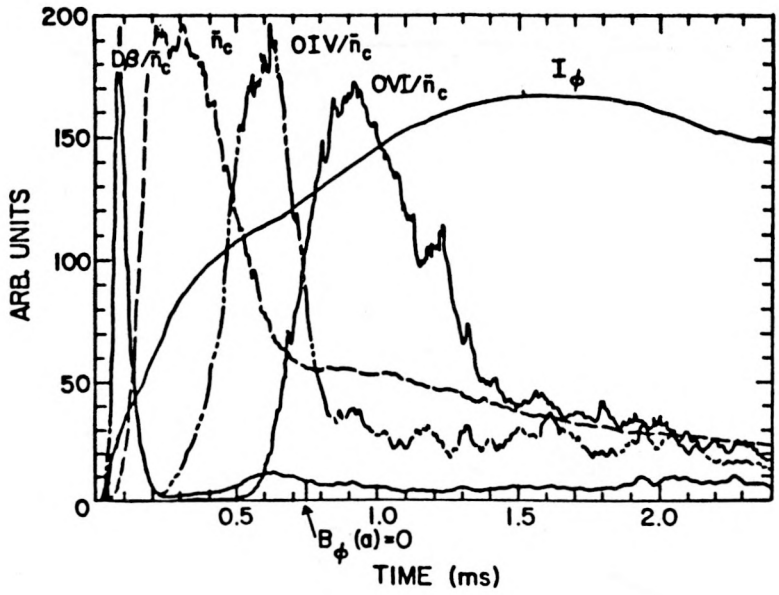

(a)

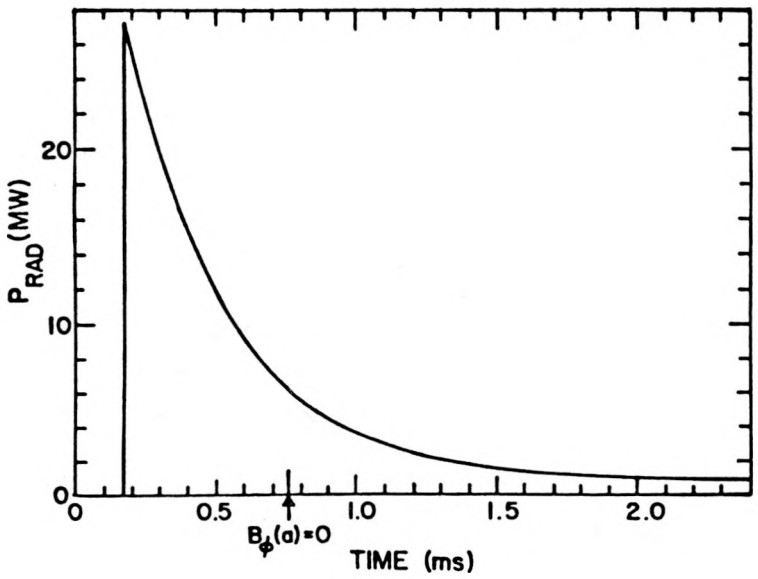

(b)

Fig. 17.

Data for 180-kA, 1.5-ms risetime case: (a) plasma current I_ϕ, line average density $\bar{n}_c$, and normalized line radiation for D_β, OIV, and OVI during start-up. (b) Bolometer power P_{RAD} during start-up.

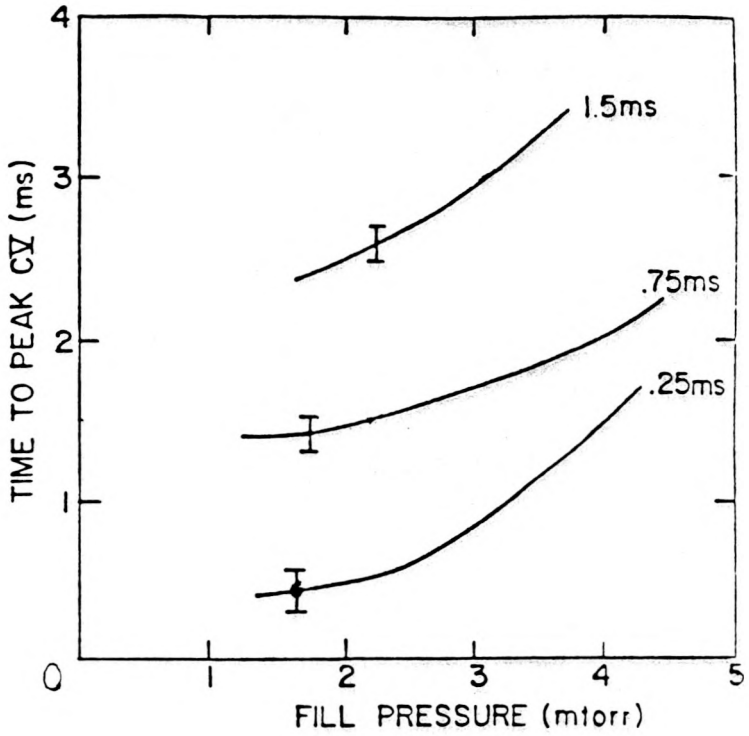

Fig. 18.
The machine time to peak CV emission for 180-kA discharges as a function of fill pressure: τ_r = 0.25, 0.75, and 1.5 ms.

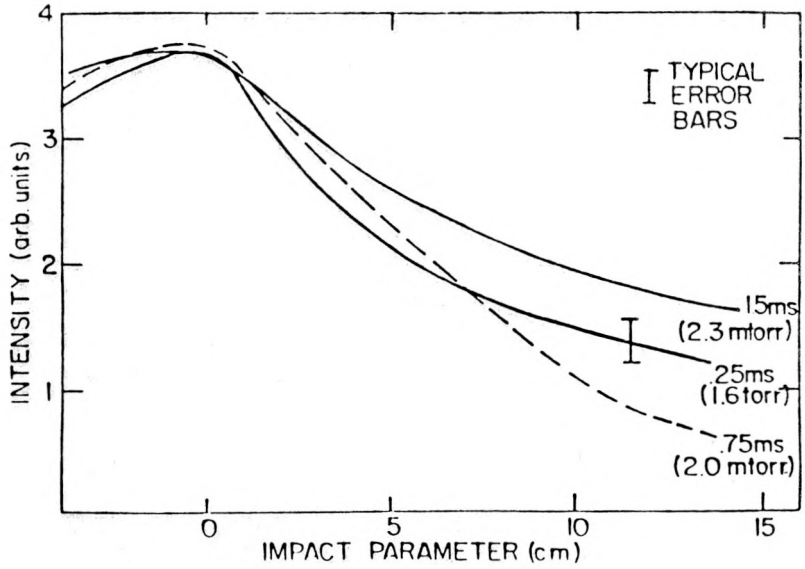

Fig. 19.
Radial profiles of CV emission at peak intensity for the three risetimes.

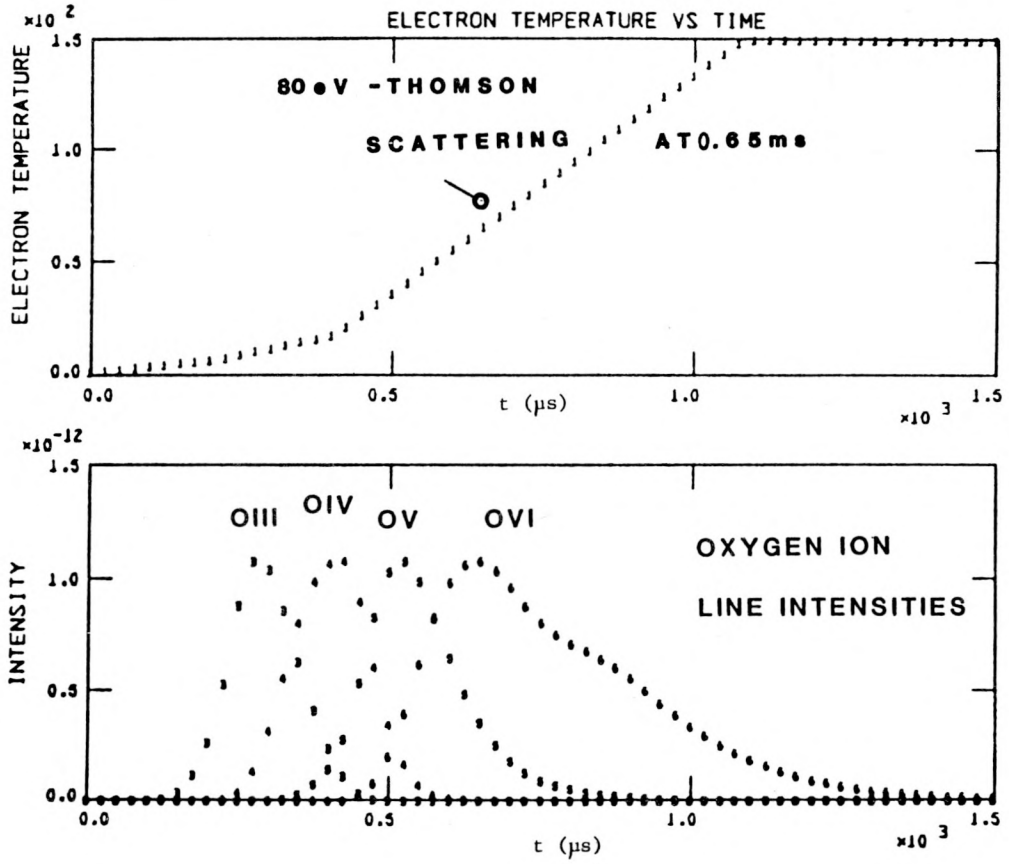

Fig. 20.

The time dependence of the electron temperatures which give a best fit with the time histories of oxygen lines calculated by a zero-dimensional computer code. The Thomson scattering temperature of 80 eV measured at 0.62 ms is indicated: discharge current ~ 180 kA, τ_r = 1.5 ms.

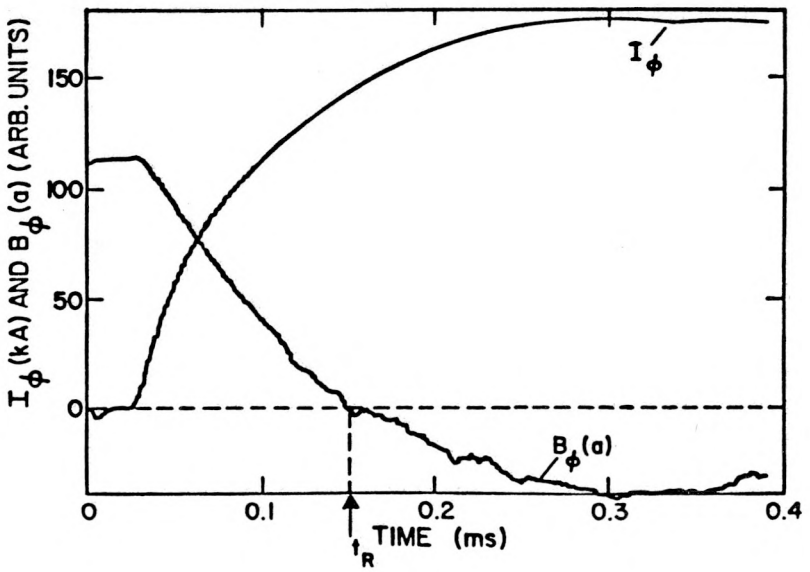

(a)

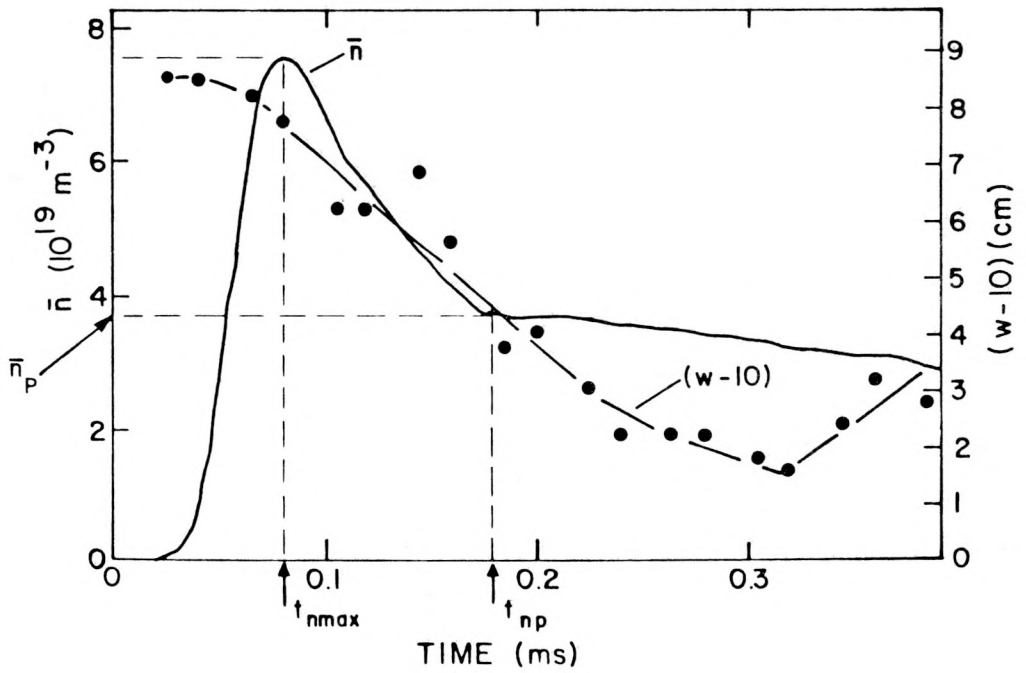

(b)

Fig. 21.

Scaled time plots of (a) I_ϕ and $B_\phi(a)$; (b) $\bar{n}$ and w for the 0.25-ms risetime. Note that $10^{}$ cm has been subtracted from all w-values before plotting.

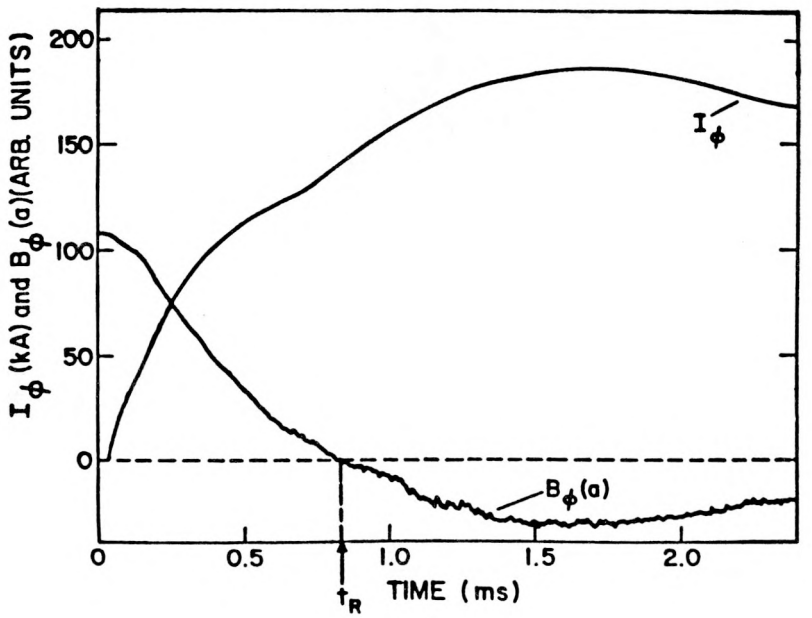

(a)

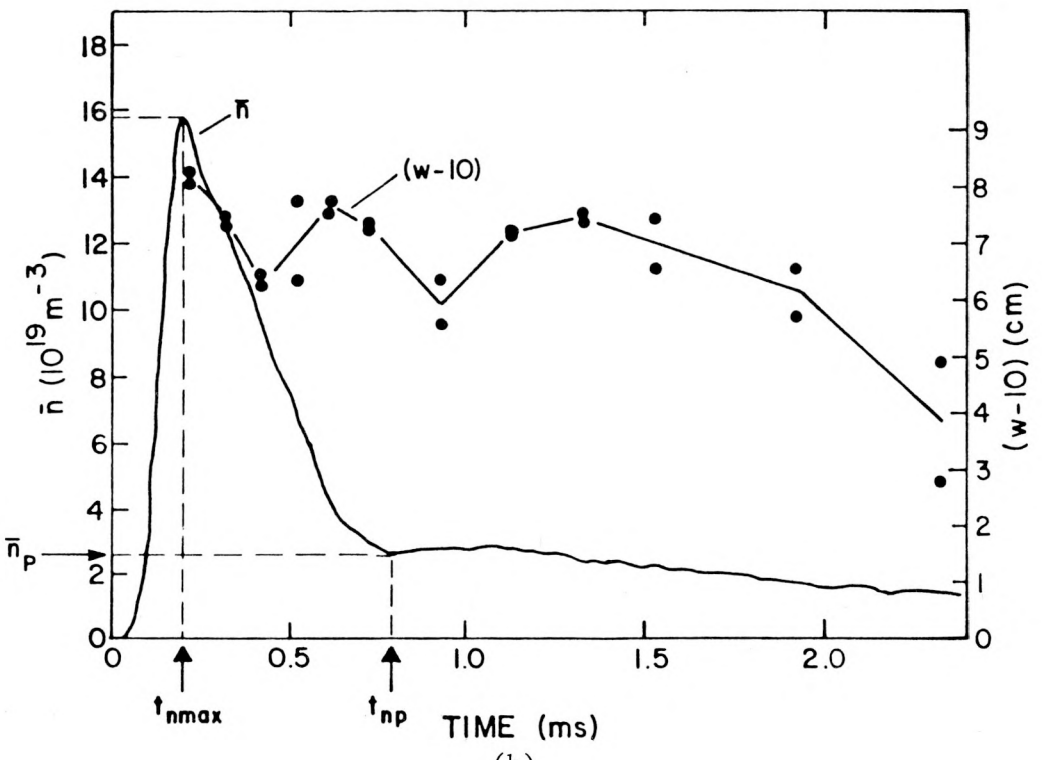

(b)

Fig. 22.

Scaled time plots of (a) I_ϕ and B_ϕ (a) and (b) $\bar{n}$ and w for the 1.5-ms risetime. Note that 10 cm has been subtracted from all w-values before plotting.

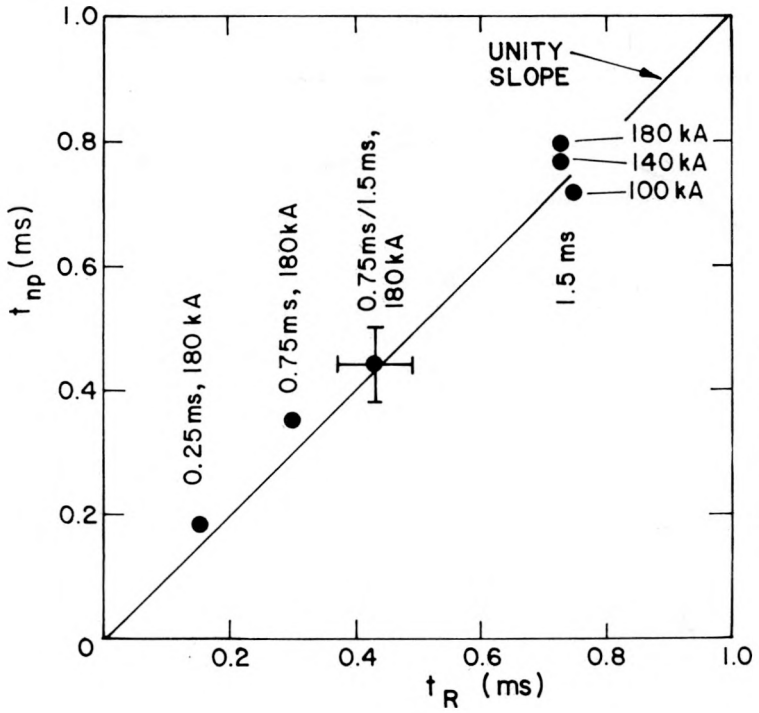

Fig. 23.
Plot of t_{np} versus t_R for the five optimized, matched-mode cases, plus one case with mismatched (0.75 ms, B_ϕ; 1.5 ms, I_ϕ) risetimes.

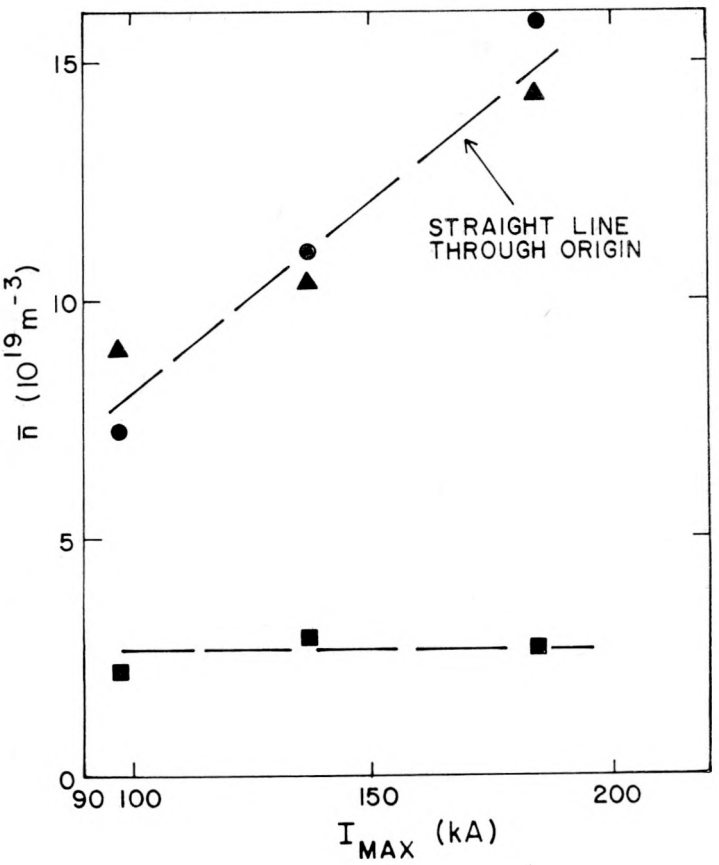

Fig. 24.
Volume-averaged density behavior as a function of I_{MAX} at 1.5-ms risetime: $\bar{n}_{MAX}$ (●), $\bar{n}_p$ ([]), and $\bar{n}(2.3)$ multiplied by a factor of 10 (Δ). Each point is an average of 10 to 20 discharges.

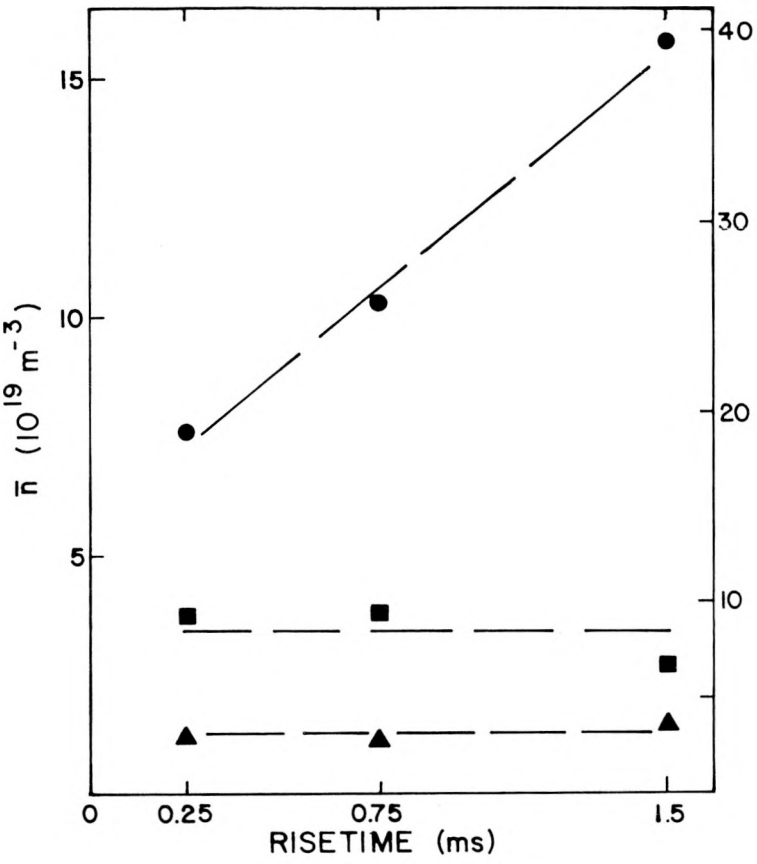

Fig. 25.

Volume-averaged density behavior as a function of risetime at 180 kA peak current: $\bar{n}_{MAX}$ (●), $\bar{n}_p$ ([]), and $\bar{n}(2.3)$ (Δ). Each point is an average of 10 to 20 discharges.

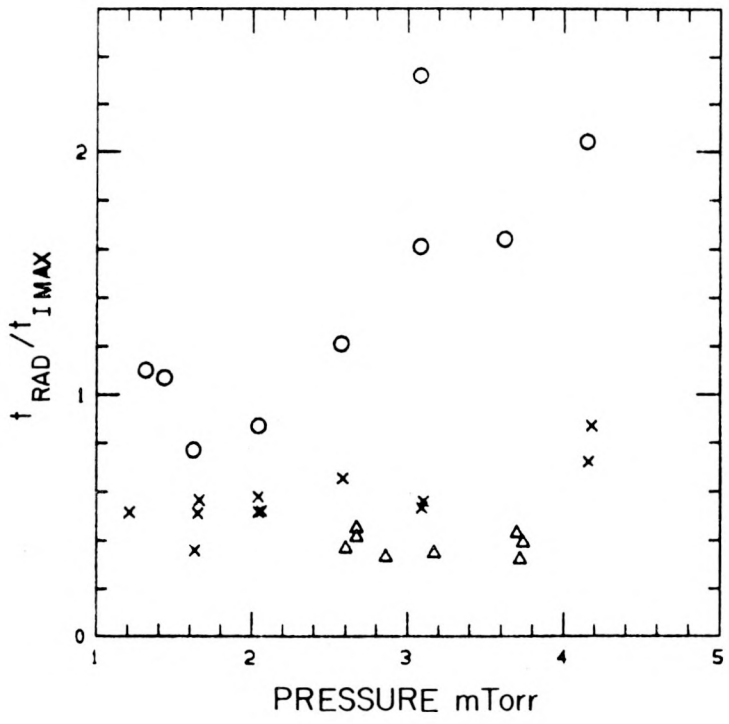

Fig. 26.

t_{RAD}/t_{MAX} versus pressure for 0.25-ms (o), 0.75-ms (x), and 1.5-ms (Δ) risetimes.

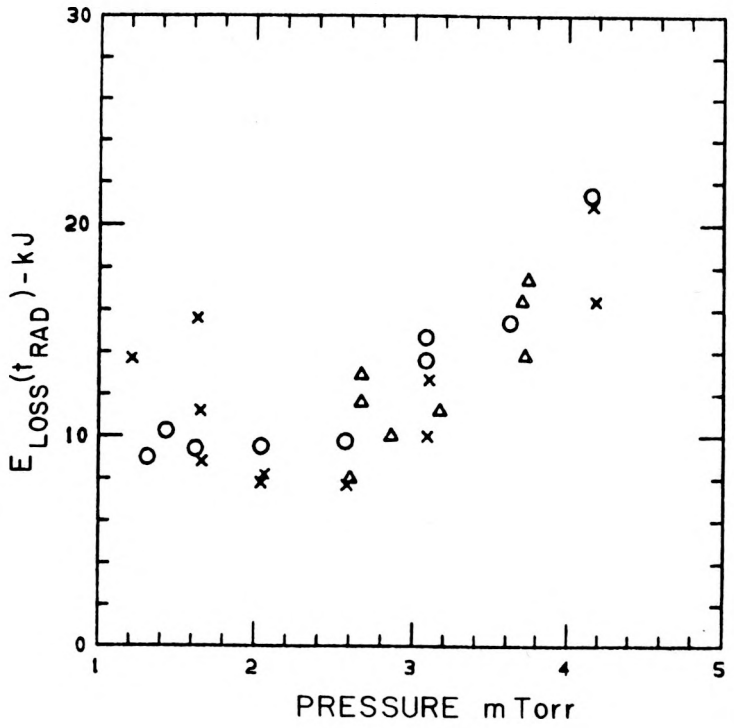

Fig. 27.

$E_{LOSS}(t_{RAD})$ versus pressure for 0.25-ms (o), 0.75-ms (x), and 1.5-ms (Δ) risetimes.

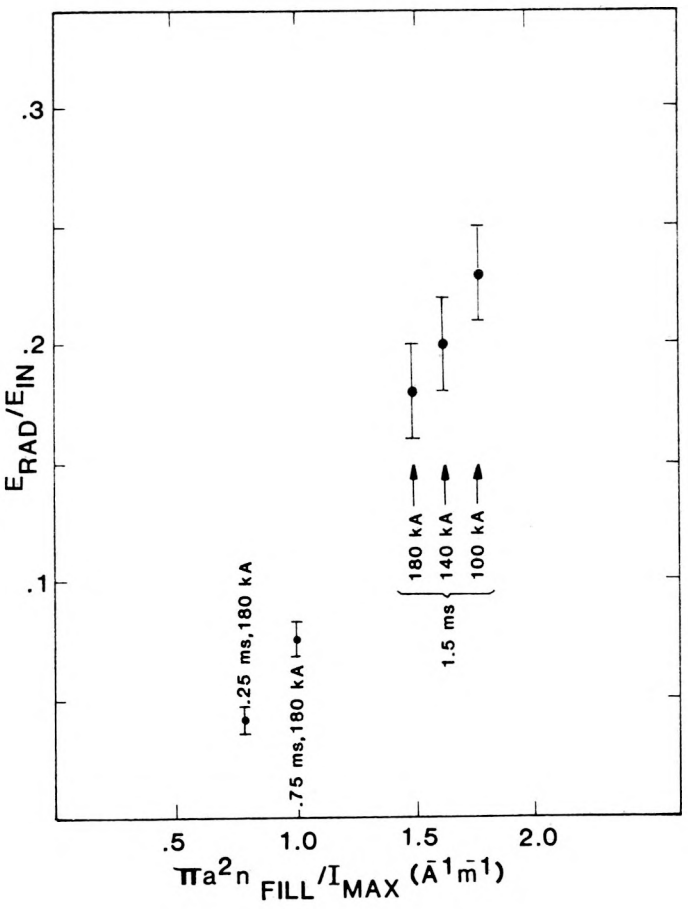

Fig. 28.

E_{RAD}/E_{IN} versus $\pi a^2 n_{FILL}/I_{MAX}$ for the five optimized, matched-mode cases.